Static and Dynamic Characteristics of In(AsSb)/GaAs Submonolayer Lasers

David Quandt, Dejan Arsenijević, André Strittmatter, and Dieter H. Bimberg, *Fellow, IEEE*

***Abstract*— The gain spectrum and modulation characteristics of ridge-waveguide laser diodes with InAs/GaAs submonolayer (SML) stacks have been investigated in detail. A comparison between active regions with intentionally altered inhomogeneous broadening is presented. The inhomogeneous broadening is controlled via Sb incorporation into the SML allowing for broader gain bandwidth and 3-D confinement of holes. In that way, the degree of charge-carrier localization can be tuned at a given wavelength. A slight performance loss at a given operation wavelength is observed due to a smaller optical overlap for the intentionally broadened gain medium. Still, bit rates up to 17 GBit/s can be obtained with the prospect for wider wavelength tunability. Multiple stacks of Sb-containing SMLs are suggested to enhance the optical overlap, which eventually allows for widely tunable quantum-dot lasers with larger modulation bandwidth.**

***Index Terms*— Submonolayer (SML), quantum dot (QD), laser diode, high-speed modulation.**

I. Introduction

HIGH density quantum-dot (QD) based lasers are of great interest due to their increased material gain and temperature stability of the threshold current in comparison to quantum-well (QW) based lasers [1]–[3]. Cyclic growth of InAs/GaAs submonolayers (SMLs) results in the formation of vertically coupled high-density Indium agglomerations in the SML stack. These have been used alternatively to Stranski-Krastanov QDs as active media in semiconductor disk lasers [4], high-power diode lasers [5] and vertical cavity surface emitting laser diodes [6]–[8]. A large modal gain and a zero linewidth enhancement factor near threshold was found by Xu *et al.* [9]. Temperature-dependent characterization of the gain of SMLs grown with molecular beam epitaxy was done by Arsenijević *et al.* [10]. A peak gain of 9.6 cm^{-1} across a temperature range of 15 °C to 65 °C and a characteristic temperature of 101 K were reported. Additionally, semiconductor optical amplifiers using SML stacks have been experimentally and theoretically investigated, showing again large modal gain as well as fast gain recovery [11], [12]. Here, we investigate static and dynamic characteristics of edge-emitting lasers with In(AsSb)/GaAs SML stacks as active medium. In particular, we compare active regions prepared with different degrees for localization of electrons and holes but with emission peaks around the same wavelength of 980 nm. This wavelength has been increasingly used for VCSELs [8], [13]–[15] due to its advantages of higher differential gain and improved temperature stability, as compared to VCSELs emitting at 850 nm [16], [17]. In a preceding report [18], we showed that with increasing Sb incorporation into the InAs/GaAs SML stack the 3D localization of holes can be further increased with the electrons confined only to the xy-plane. A recent spectroscopic analysis of binary InAs/GaAs SMLs revealed such a heterodimensionality in the localization properties of electrons and holes. With holes being stored in 3D localization potentials and electrons being free to move in the xy-plane of the SML stack, high-speed operation was predicted [19]. An increase of the heterodimensionality of the active region is therefore interesting in the framework of the aforementioned model. We have demonstrated that the addition of an Sb flush to the SML growth cycle leads to QD-like emission in photoluminescence (PL) measurements [18]. This is caused by an enhanced localization of the hole wavefunction and a simultaneous delocalization of the electron wavefunction, thus increasing the heterodimensionality. Further investigations showed that the Sb incorporation can be modeled by a Langmuir-type adsorption model and the existence of an upper limit for the GaAs spacer between the InAs insertions of about 1.8 - 1.9 MLs to enable the enhanced hole-localization [20]. In this paper, we investigate the static and dynamic properties of edge emitting lasers utilizing single InAs/GaAs-SML stacks grown with and without Sb flush.

II. Laser Structure, Fabrication and Characterization

The laser structures were grown by low-pressure metalorganic chemical vapor deposition (MOCVD). A single SML stack is employed as active region and embedded into a 600-nm-thick $Al_{0.15}GaAs$ waveguide region, sandwiched between two 2-μm-thick $Al_{0.25}GaAs$ cladding layers. A 200-nm-thick GaAs p^{+}-contact layer is used as cap.

Manuscript received December 9, 2018; revised March 25, 2019; accepted April 12, 2019. Date of publication April 30, 2019; date of current version May 22, 2019. The research for this article has been financially supported by the CRC 787 "Semiconductor Nanophotonics" of the Deutsche Forschungsgemeinschaft. *(Corresponding author: David Quandt.)*

D. Quandt was with the Institute of Solid-State Physics, Technische Universität Berlin, 10623 Berlin, Germany. He is now with II-VI Laser Enterprise GmbH, 8045 Zurich, Switzerland (e-mail: dquandt@physik.tu-berlin.de).

D. Arsenijević was with the Institute of Solid-State Physics, Technische Universität Berlin, 10623 Berlin, Germany. He is now with Sicoya GmbH, 12489 Berlin, Germany (e-mail: dejan.arsenijevic@sicoya.de).

A. Strittmatter is with the Institut für Physik, Otto-von-Guericke Universität Magdeburg, 39106 Magdeburg, Germany (e-mail: andre.strittmatter@ovgu.de).

D. H. Bimberg is with the Center of NanoPhotonics, Institute of Solid-State Physics, Technische Universität Berlin, 10623 Berlin, Germany, and also with the Bimberg Chinese-German Center for Green Photonics, Chinese Academy of Sciences, CIOMP, Changchun 130033, China (e-mail: bimberg@physik.tu-berlin.de).

Color versions of one or more of the figures in this paper are available online at http://ieeexplore.ieee.org.

Digital Object Identifier 10.1109/JQE.2019.2913877

TABLE I
STRUCTURAL AND OPTICAL PROPERTIES OF THE SML STACKS

Deposition cycles	12	6
Average composition	$In_{0.17}GaAs$	$In_{0.13}GaAsSb_{0.14}$[1]
SML stack thickness (nm)	8.1	2.5
PL emission wavelength (nm)	988	977

The basic growth parameters of the SML stacks can be found in [18]. Composition, distances and deposition cycles of the SML stacks are tuned to yield the same emission wavelength. The thickness and composition can be estimated from calibration samples. Note that it is only possible to determine the In+Sb content. The structural properties as well as the emission wavelength obtained from PL measurements are given in Table I.

For the determination of the basic laser characteristics (internal quantum efficiency, optical losses and characteristic temperature), 100-μm-broad stripes were defined by etching through the top-contact layer. A Ti/Pt/Au metallization is used as p-side top contact while Ni/AuGe/Au metallization on the substrate backside is employed for the n-side contact. Laser facets were prepared by wafer cleavage and left uncoated. Self-heating effects during laser operation were suppressed using pulsed excitation at 1 kHz repetition rate and 800 ns pulse length.

Gain measurements as well as small- and large-signal modulation measurements were performed on narrow-stripe lasers. Deeply-etched 3.3-μm to 3.8-μm-wide stripes, were fabricated by UV photolithography and dry etching. The etching was stopped above the active region (~100 nm). Surface planarization was obtained by spin-coating with benzocyclobutene (BCB). The cavity length is 700 μm. In contrast to the broad-area devices, the n-contact is placed on the top-side.

III. STATIC CHARACTERISTICS

A. Broad-Area Lasers

The variable length method was applied to determine static lasing characteristics from pulsed mode L-I-V measurements. The laser lengths varied from 1 mm to 3 mm. Linear regression of the L-I-V curve above lasing threshold yields the external differential quantum efficiencies and threshold currents of the devices. The lasing wavelength is red-shifted by about 5 nm compared to the respective PL measurement for lasers of 1 mm length.

Fig. 1 shows the inverse differential quantum efficiency versus laser cavity length. The obtained data points have been fitted by the relation [21]

$$\frac{1}{\eta_d} = \frac{1}{\eta_i} \cdot \left(1 + \frac{\alpha_i}{\log(\frac{1}{R})} \cdot L\right) \tag{1}$$

where η_d is the differential quantum efficiency, η_i is the internal quantum efficiency, α_i is the optical loss, R denotes

[1]The quaternary composition is determined by a combination of X-ray diffraction and grazing-incidence X-ray fluorescence measurements [20].

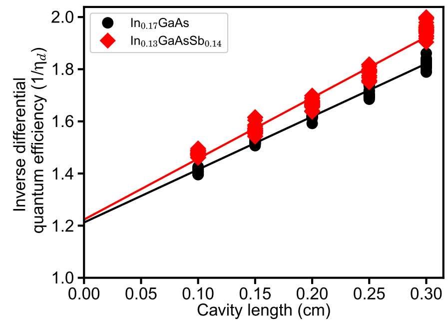

Fig. 1. Cavity-length-dependent inverse differential quantum efficiency of broad-area lasers. Filled symbols are the values extracted from the L-I-V measurements, solid lines are least-squares fits to equation (1).

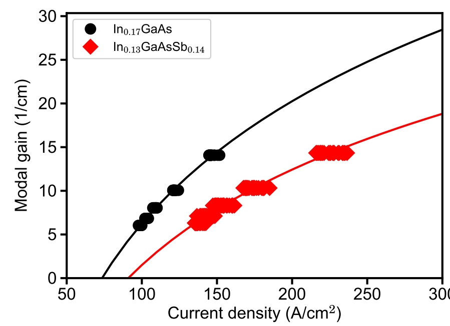

Fig. 2. Modal gain with respect to the threshold current density of the broad-area lasers. Values extracted from the L-I-V measurements are shown as filled symbols and least-squares fits as to equation (2) as solid lines.

the facet reflectivity and L is the laser length. The addition of Sb results in an increase of the internal losses from 2.02 ± 0.04 cm^{-1} to 2.30 ± 0.05 cm^{-1}, which is about 14%. Meanwhile the internal quantum efficiency remains constant with 0.82 ± 0.01 for both active regions.

To determine the transparency current density and the gain coefficient, the necessary modal gain for each laser length was plotted with respect to the threshold current density. The logarithmic gain approximation [22] was then used to extract the transparency current density and the gain parameter (see fig. 2).

$$G(J_{thr}) = G_0 \cdot \ln\left(\eta_i \frac{J_{thr}}{J_{tr}}\right) \tag{2}$$

J_{thr} is the threshold current density, j_{tr} is the transparency current density, ΓG_0 is the gain parameter. η_i is obtained from the previous fit to equation (1).

We find an increase of the transparency current density from 60.6 ± 0.3 A/cm^2 without Sb to 74.3 ± 0.6 A/cm^2 with Sb. The gain parameter decreases from 20.2 ± 0.2 cm^{-1} to 15.8 ± 0.2 cm^{-1}. The decreasing performance of the InGaAsSb-SML laser is primarily due to the reduced vertical dimension of the stack causing an reduced fill factor. With the relatively small change in internal optical losses the increase in transparency current must be assigned to an effective increase of the number of recombination centers by about 22 %,

TABLE II
BROAD AREA RESULTS

	$In_{0.17}GaAs$	$In_{0.13}GaAsSb_{0.14}$
Lasing wavelength (nm)	990 ± 5	979 ± 3
η_i	0.82 ± 0.01	0.82 ± 0.01
α_i (cm^{-1})	2.02 ± 0.04	2.30 ± 0.05
j_{tr} (A/cm^2)	60.6 ± 0.3	74.3 ± 0.6
ΓG_0 (cm^{-1})	20.2 ± 0.2	15.8 ± 0.2
T_0	110.2 ± 7.4	88.9 ± 4.7

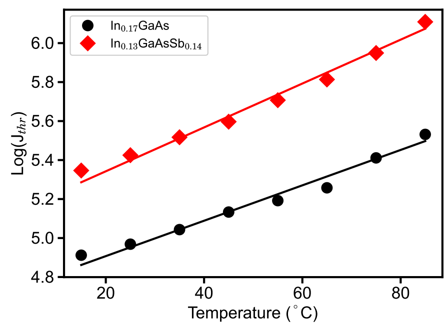

Fig. 3. Temperature dependence of the threshold current density for the broad-area lasers. T_0 is extracted by fitting to equation (3) (solid lines).

judging from the increase of the transparency current density (compare table II).

Fig. 3 shows the logarithmic threshold current as a function of temperature for lasers of 1 mm length. In order to obtain the characteristic temperature we performed a least-squares fit to the equation [22]

$$J_{thr} = J_0 \cdot \exp\left(\frac{T}{T_0}\right) \tag{3}$$

J_0 is the threshold current density at 0 K, T is the temperature and T_0 is the characteristic temperature. We find a decrease of the characteristic temperature from 110.2 ± 7.4 K to 88.9 ± 4.7 K. As the addition of Sb to the growth sequence is expected to enhance delocalization of the electrons [18], a larger electron leakage current from the SML stack and a subsequent decrease of the temperature stability is expected.

The internal parameters obtained from the broad-area lasers are summarized in table II. Overall, the addition of Sb slightly decreases the temperature stability and the modal gain. The increased threshold current can be explained by the high density ($\sim 10^{12}$ cm^{-2}) of 0D localization centers contained in the In(AsSb)/GaAs SML stack [18]. Calculations suggest that for given size broadening within a QD ensemble the QD density to achieve similar or higher gain than with a single QW at lower pump current density is optimum around low 10^{11} cm^{-2} range [23], [24].

B. Narrow-Stripe Lasers

High-resolution optical spectra have been measured from two narrow-stripe lasers under dc bias. The laser without Sb in the active region had a 0.5 μm wider ridge waveguide than the laser with Sb. Fig. 4 shows the L-I-V curves of both lasers.

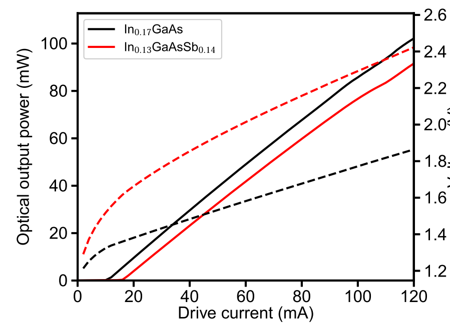

Fig. 4. L-I-V curves of both narrow stripe lasers. Solid lines are optical output power vs. drive current while dashed lines are the corresponding voltages.

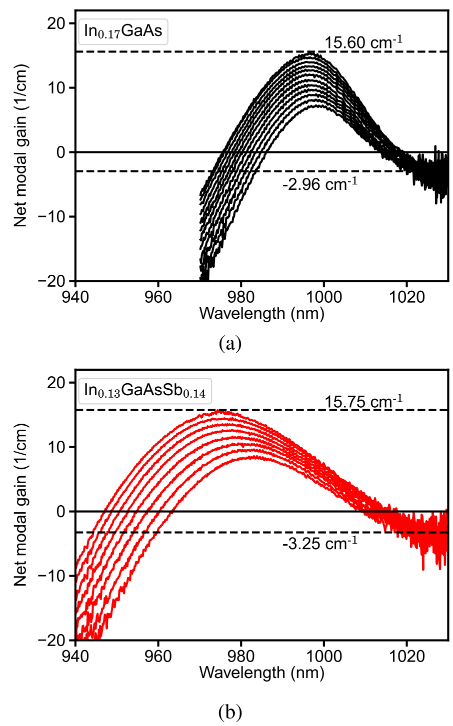

Fig. 5. Gain of the narrow-stripe lasers between $0.8\times I_{thr}$ and $0.95\times I_{thr}$ as obtained from a nonlinear least-squares fitting method.

The gain characteristics have been investigated by utilizing a nonlinear least-squares fitting method [25] at drive currents between 0.8 and $0.95\times I_{thr}$ in steps of $0.05\times I_{thr}$. The obtained gain spectra are shown in Fig. 5. As expected from PL measurements [18], the FWHM of the gain spectrum significantly increases with the Sb content in the active region. For the investigated lasers it increases by more than 50% from 23.7 ± 0.3 nm for the $In_{0.17}GaAs$ SML stack to 41.6 ± 0.2 nm for $In_{0.13}GaAsSb_{0.14}$. The maximum modal gain is determined by the mirror losses and stays virtually constant at 15.60 and 15.75, respectively. The internal loss of the lasers has been determined by assuming zero modal gain at long wavelengths [26] to 3.0 ± 0.4 cm^{-1} without and 3.3 ± 0.5 cm^{-1} with Sb.

Due to the larger stripe width, the laser without Sb exhibits signs of weak multi modal behavior. This is also found in the small-signal measurements as will be shown later.

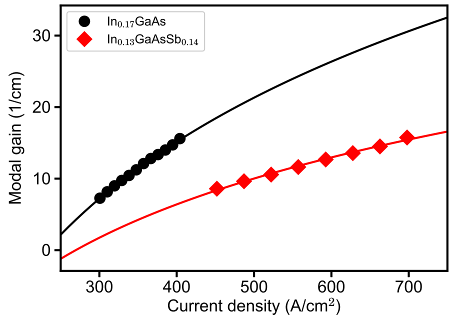

Fig. 6. Peak modal gain with respect to the current density as determined from high-resolution optical spectra (see Fig. 5). Solid lines are fits to equation (2).

TABLE III
NARROW STRIPE RESULTS

	$In_{0.17}GaAs$	$In_{0.13}GaAsSb_{0.14}$
Lasing wavelength (nm)	996 ± 0.2	975 ± 1
I_{th} (mA)	10.52 ± 0.02	15.86 ± 0.01
ΔG	25.9 ± 0.3	42.9 ± 0.2
G (cm^{-1})	27.6 ± 0.3	16.2 ± 0.5
α_i (cm^{-1})	3.0 ± 0.4	3.3 ± 0.5
Γ	0.0157	0.0048
g_{mat} (cm^{-1})	1572 ± 29	2696 ± 145

In order to get a measure of the saturation behavior and the material gain of the lasers, the peak modal gain of each measurement has been analyzed with respect to the drive currents (Fig. 6). Again, the logarithmic gain approximation is used to determine the gain coefficient which decreases from 27.6 ± 0.3 cm^{-1} to 16.2 ± 0.5 cm^{-1}.

For the material gain, the confinement factor of each laser structure was calculated using the effective index method [27]. The material gain is calculated according to

$$G = \Gamma \cdot g_{mat} - \alpha \tag{4}$$

G is the modal gain coefficient as from the fit with the logarithmic gain approximation, Γ is the confinement factor, α is the internal optical loss and g_{mat} is the material gain. For the latter, we find an increase by about ∼72%, from 1572 ± 29 cm^{-1} without Sb to 2696 ± 145 cm^{-1} with Sb.

The parameters for the narrow-stripe lasers are summarized in table III.

IV. DYNAMIC CHARACTERISTICS

A. Small-Signal Modulation Response

In order to analyze the dynamic properties of the lasers, small-signal response curves (S_{21}) were measured. The emitted laser light was collected by a tapered single-mode HI-980 fiber which was connected to a New Focus 1014 45-GHz single-mode detector and a HP 8722C 40 GHz vector network analyzer. The obtained curves were fitted with a three-pole

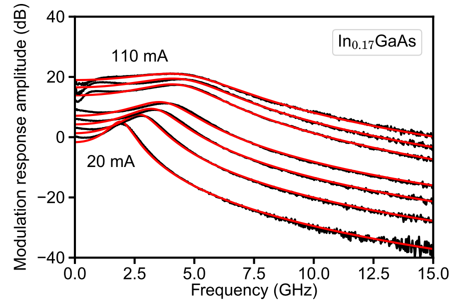

(a)

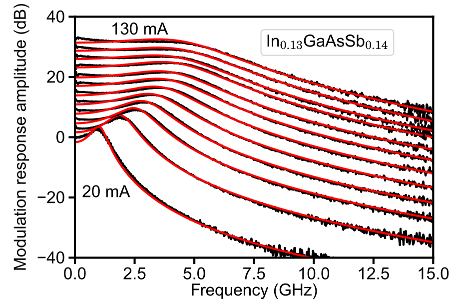

(b)

Fig. 7. Small-signal response curves for the two lasers at their maximum bandwidth. Solid red lines are the fits to equation (5). Curves have been vertically shifted for clarity. Minimum and maximum used drive currents are shown.

TABLE IV
PARAMETERS EXTRACTED FROM SMALL-SIGNAL MEASUREMENTS

	$In_{0.17}GaAs$	$In_{0.11}GaAsSb_{0.09}$
D-factor (GHz/$\sqrt{\text{mA}}$)	0.626 ± 0.008	0.532 ± 0.002
K-factor (ns)	0.861 ± 0.034	1.096 ± 0.032
MCEF-factor (GHz/$\sqrt{\text{mA}}$)	0.90 ± 0.02	0.75 ± 0.01
$\partial g/\partial n$ (10^{-16} cm^2)	5.1 ± 0.2	3.2 ± 0.3
τ_p (ps)	6.48 ± 0.52	6.27 ± 0.58
ε (10^{-17} cm^3)	5.9 ± 0.5	5.3 ± 0.5
τ_{max} (ps)	7	15
Γ/V (10^5)/cm^3)	7.3	8.3

transfer function [28].

$$H_f = \frac{f_r^4}{(f_r^2 - f^2)^2 + \frac{f^2\gamma^2}{4\pi^2}} \cdot \frac{1}{1 + 4\pi^2 f^2 \tau^2} \tag{5}$$

f_r is the resonance frequency, γ is the damping factor, τ is the carrier transport time and f is the measurement frequency. Fig. 7 shows the small-signal response curves at increasing bias currents for both lasers. Note that the laser without Sb shows an additional resonance peak at low frequencies for bias currents of 70 mA and larger. This is most likely caused by the multi modal characteristics due to the larger stripe width.

The maximum carrier transport time τ_{max} for each laser has been added to table IV. As it is in the order of tens of picoseconds in all cases, we conclude that the maximum modulation bandwidth is not limited by it.

From each curve, the -3-dB frequency with respect to the square root of the current above threshold can be extracted,

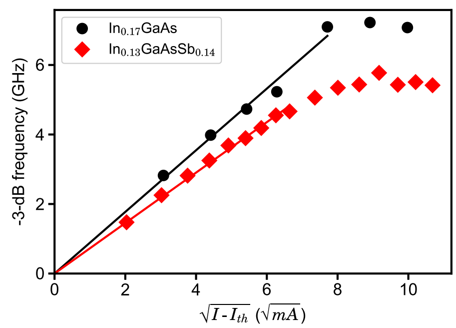

Fig. 8. −3-dB frequency with respect to the square root of the bias current above threshold. The solid symbols are the extracted values and the solid lines are the fits according to equation (6).

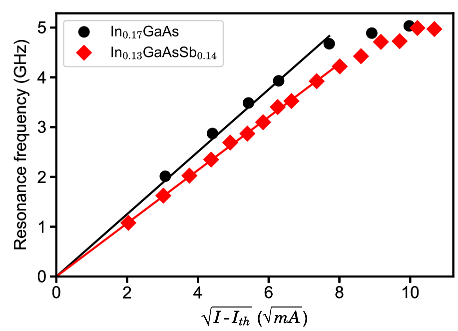

Fig. 9. Resonance frequency with respect to the square root of the bias current above threshold. The solid symbols are the extracted values and the solid lines are the fits according to equation (7).

allowing for the determination of the modulation current efficiency factor (MCEF) by fitting the equation [29] (see Fig. 8)

$$f_{3dB} = MCEF \cdot \sqrt{I - I_{th}} \tag{6}$$

Here, a decrease from 0.90 ± 0.02 GHz/$\sqrt{\text{mA}}$ ($In_{0.17}GaAs$) to 0.75 ± 0.01 GHz/$\sqrt{\text{mA}}$ ($In_{0.13}GaAsSb_{0.14}$) is determined.

In order to better understand the reason for this decrease, the small-signal measurements are further analyzed, starting with the extraction of the D-Factor [30], [31].

$$f_r = D \cdot \sqrt{I - I_{th}} \tag{7}$$

with

$$D = \frac{1}{2\pi}\sqrt{\frac{\eta_i \Gamma \upsilon_g}{qV}\frac{\partial g/\partial n}{\chi}} \tag{8}$$

υ_g is the group velocity, q is the elementary charge, V is the volume of the active region, $\partial g/\partial n$ is the differential gain and χ is the transport factor.

Fig. 9 shows the resonant frequency with respect to the square root of the current above threshold and the respective fit to equation 7. Starting from a value of 0.626 ± 0.008 GHz/$\sqrt{\text{mA}}$, the D-factor decreases to 0.532 ± 0.002 GHz/$\sqrt{\text{mA}}$ if Sb is contained in the active region. Neglecting transport effects ($\chi \sim 1$) for simplicity allows for the extraction of the differential gain. We find that Sb decreases the differential gain from $(5.1 \pm 0.2)\cdot 10^{-16}$ cm^2 to $(3.2 \pm 0.3)\cdot 10^{-16}$ cm^2.

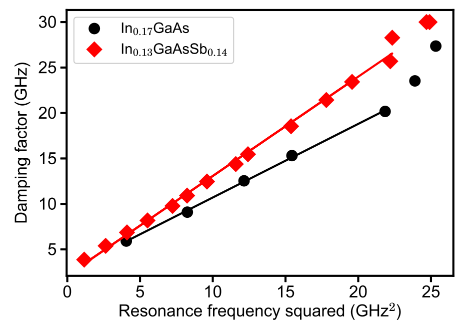

Fig. 10. Damping factor with respect to the squared resonance frequency. The K-factor is determined by a fit to equation (9).

Additionally, the K-factor is obtained via the relation [32]

$$\gamma = K \cdot f_r^2 + \gamma_0 \tag{9}$$

with

$$K = 4\pi^2\left(\tau_p + \frac{\varepsilon\chi}{\upsilon_g \frac{\partial g}{\partial n}}\right) \tag{10}$$

ε is the gain compression factor, χ is the transport factor and $\partial g/\partial n$ is the differential gain. τ_p is the photon lifetime in the cavity and it is defined as [33]

$$\tau_p = \frac{1}{\upsilon_g\left(\alpha_i + \frac{1}{L}\ln\left(\frac{1}{R}\right)\right)} \tag{11}$$

The group velocity of light is estimated from the mode spacing in the high-resolution optical spectra.

Fig. 10 shows the damping factor with respect to the square of the resonance frequency and the respective fit to equation 9. Adding Sb results in an increase of the K-factor from 0.861 ± 0.034 ns to 1.096 ± 0.032 ns. The differential gain, which was extracted from the D-factor, allows for the calculation of the gain compression factor (again with $\chi \sim 1$). Here we find approximately equal values of $(5.9 \pm 0.5)\cdot 10^{-17}$ cm^3 for the $In_{0.17}GaAs$ SML stack and $(5.3 \pm 0.5)\cdot 10^{-17}$ cm^3 for the $In_{0.13}GaAsSb_{0.14}$ SML stack.

All parameters extracted from the small-signal modulation response measurements are summarized in table IV. Additionally the ratio of the confinement factor to the volume of the active region is included.

Judging from this, the decrease of the small-signal modulation bandwidth upon the addition of Sb is most likely rooted in the decrease of the differential gain due to the increased spectral broadening upon the addition of Sb and the reduced optical confinement factor. This corresponds to the static measurements, where the modal gain is also limited by the confinement factor and increased gain distribution despite the larger material gain (compare table III).

B. Large-Signal Modulation

Data-transmission capabilities of the lasers were probed by direct-modulation signals with a non-return-to-zero (NRZ) pseudo-random binary sequence (PRBS) of 2^7-1 bit length. The lasers were biased at currents yielding the maximum

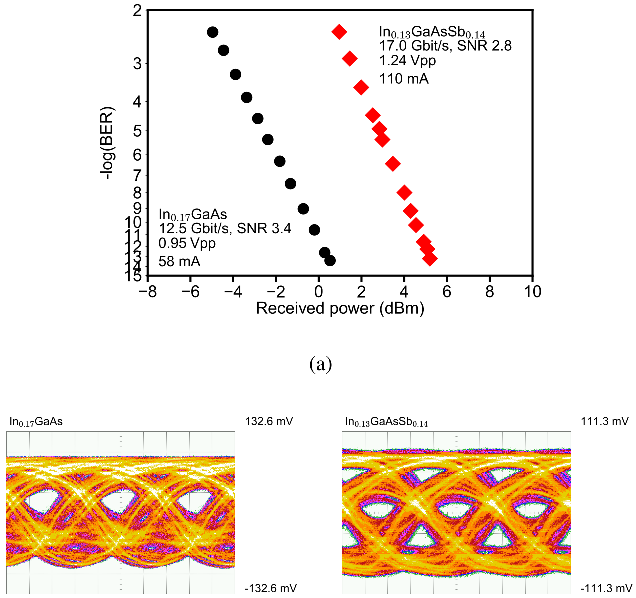

(a)

(b)

Fig. 11. BER curves (a) and eye diagrams (b) for the two lasers. The eye diagrams are obtained for received optical powers at error-free threshold.

−3-dB frequency while retaining a single resonance peak under small-signal modulation conditions (58 mA, for the laser without Sb and 110 mA for the laser with Sb). The output of an SHF 12100 B Bit Pattern Generator was amplified by means of a broadband SHF 804TL RF amplifier. Modulation swings were adjusted to 0.95 and 1.24 Vpp accordingly. On the detection side error ratios were measured by means of an SHF 11100 B Error Analyzer, while eye diagrams were acquired with a Keysight DSAX93204A 80 GSa/s real-time oscilloscope. By using a custom made 28-GHz limiting photoreceiver (Finisar), elimination of signal overshoot and high intensity noise was achieved being prerequisite for this kind of measurement. The bit error rate (BER) curves and the corresponding eye diagrams at the error-free threshold of $BER < 10^{-12}$ are displayed in Fig. 11.

For the laser with a $In_{0.17}GaAs$ SML stack, we achieved a maximum error-free bit rate of 12.5 Gbit/s with an eye signal-to-noise-ratio (SNR) of 3.4 at a drive current of 58 mA. In comparison, the laser using the $In_{0.11}GaAsSb_{0.09}$ SML stack showed a maximum bit rate of 17 Gbit/s and a SNR of 2.8. The laser with Sb has to be driven at a larger bias current to achieve the same -3-dB frequency as the laser without Sb and thus has a larger output power. The larger output power directly translates to the larger maximum bit rate observed by us as it matches better with the optimal gain of the photoreceiver.

V. Conclusion

In conclusion, we have studied the characteristics of lasers utilizing single InAs/GaAs SML stacks grown with and without an Sb flush as active media. Our previously demonstrated enhanced QD formation within the SML active region due to Sb incorporation yields both higher material gain and broader gain bandwidth. The laser dynamics of lasers with Sb-containing SML stacks is limited by a reduced modal peak gain and larger spectral gain spreading causing larger drive currents for a given small-signal modulation bandwidth. By increasing the number of SML stacks in the laser active region the modal peak gain will be enhanced which enables an increased small-signal modulation bandwidth. Although multiple SML stacks are in principle possible [4], [18], [20], their number and vertical separation has to be optimized with regard to laser performance which is subject of on-going work. In other device types, the broadened gain spectrum might yield advantages, for instance in mode-locked lasers [34], [35] and temperature-stable VCSELs [36], [37].

Acknowledgment

The authors D. Q. and A. S. would like to thank the CRC 787 "Semiconductor Nanophotonics" of the Deutsche Forschungsgemeinschaft for financial support.

References

[1] M. Asada, Y. Miyamoto, and Y. Suematsu, "Gain and the threshold of three-dimensional quantum-box lasers," *IEEE J. Quantum Electron.*, vol. 22, no. 9, pp. 1915–1921, Sep. 1986.

[2] N. Kirstaedter *et al.*, "Gain and differential gain of single layer InAs/GaAs quantum dot injection lasers," *Appl. Phys. Lett.*, vol. 69, no. 9, p. 1226, Jun. 1996.

[3] D. Bimberg, N. Kirstaedter, N. Ledentsov, Z. Alferov, P. Kop'ev, and V. Ustinov, "InGaAs-GaAs quantum-dot lasers," *IEEE J. Sel. Topics Quantum Electron.*, vol. 3, no. 2, pp. 196–205, Apr. 1997.

[4] T. D. Germann *et al.*, "High-power semiconductor disk laser based on In As / Ga As submonolayer quantum dots," *Appl. Phys. Lett.*, vol. 92, no. 10, 2008, Art. no. 101123.

[5] A. E. Zhukov *et al.*, "3.9 W CW power from sub-monolayer quantum dot diode laser," *Electron. Lett.*, vol. 35, no. 21, pp. 1845–1847, Oct. 1999.

[6] F. Hopfer *et al.*, "Single-mode submonolayer quantum-dot vertical-cavity surface-emitting lasers with high modulation bandwidth," *Appl. Phys. Lett.*, vol. 89, no. 14, 2006, Art. no. 141106.

[7] N. N. Ledentsov *et al.*, "Submonolayer quantum dots for high speed surface emitting lasers," *Nanosc. Res. Lett.*, vol. 2, no. 9, pp. 417–429, Sep. 2007.

[8] A. Mutig *et al.*, "Temperature-dependent small-signal Analysis of high-speed high-temperature stable 980-nm VCSELs," *IEEE J. Sel. Topics Quantum Electron.*, vol. 15, no. 3, pp. 679–686, May/Jun. 2009.

[9] Z. Xu, D. Birkedal, M. Juhl, and J. M. Hvam, "Submonolayer InGaAs / GaAs quantum-dot lasers with high modal gain and zero-linewidth enhancement factor," *Appl. Phys. Lett.*, vol. 85, no. 15, 2004, Art. no. 3259.

[10] D. Arsenijevic, C. Liu, A. Payusov, M. Stubenrauch, and D. Bimberg, "Temperature-dependent characteristics of single-mode InAs submonolayer quantum-dot lASERS," *IEEE Photon. Technol. Lett.*, vol. 24, no. 11, pp. 906–908, Jun. 2012.

[11] B. Herzog *et al.*, "Fast gain and phase recovery of semiconductor optical amplifiers based on submonolayer quantum dots," *Appl. Phys. Lett.*, vol. 107, no. 20, 2015, Art. no. 201102.

[12] B. Lingnau *et al.*, "Ultrafast gain recovery and large nonlinear optical response in submonolayer quantum dots," *Phys. Rev. B, Condens. Matter*, vol. 94, no. 1, Jul. 2016, Art. no. 014305.

[13] C. K. Lin, A. Tandon, K. Djordjev, S. W. Corzine, and M. R. T. Tan, "High-speed 985 nm bottom-emitting VCSEL Arrays for chip-to-chip parallel optical interconnects," *IEEE J. Sel. Topics Quantum Electron.*, vol. 13, no. 5, pp. 1332–1339, Sep. 2007.

[14] A. Mutig *et al.*, "120° 20 Gbit/s operation of 980 nm VCSEL," *Electron. Lett.*, vol. 44, no. 22, p. 1305, Sep. 2008.

[15] A. Mutig *et al.*, "Modulation characteristics of high-speed and high-temperature stable 980 nm range VCSELs operating error free at 25 Gbit/s up to 85°C," *IEEE J. Sel.Topics Quantum Electron.*, vol. 17, no. 6, pp. 1568–1575, Jul. 2011.

[16] L. A. Buckman Windover *et al.*, "Parallel-optical interconnects >100 gb/s," *J. Lightw. Technol.*, vol. 22, no. 9, pp. 2055–2063, Sep. 2004.

[17] L. Schares *et al.*, "Terabus: Terabit/second-class card-level optical interconnect technologies," *IEEE J. Sel. Topics Quantum Electron.*, vol. 12, no. 5, pp. 1032–1043, Oct. 2006.

[18] D. Quandt *et al.*, "Strong charge-carrier localization in InAs/GaAs submonolayer stacks prepared by Sb-assisted metalorganic vapor-phase epitaxy," *Phys. Rev. B, Condens. Matter*, vol. 91, no. 23, Jun. 2015, Art. no. 235418.

[19] S. Harrison *et al.*, "Heterodimensional charge-carrier confinement in stacked submonolayer InAs in GaAs," *Phys. Rev. B, Condens. Matter*, vol. 93, no. 8, Feb. 2016, Art. no. 085302.

[20] D. Quandt, J. Bläsing, and A. Strittmatter, "Analysis of InAsSb/GaAs submonolayer stacks," *J. Cryst. Growth*, vol. 494, pp. 1–7, Jul. 2018.

[21] K. Petermann, *Laser Diode Modulation and Noise*. Dordrecht, The Netherlands: Kluwer Academic Publishers, 1988.

[22] J. S. Osinski, P. Grodzinski, Y. Zou, and P. D. Dapkus, "Threshold current analysis of compressive strain quantum well lasers," *IEEE J. Quantum Electron.*, vol. 29, no. 6, pp. 1576–1585, Jun. 1993.

[23] A. E. Zhukov *et al.*, "Gain characteristics of quantum dot injection lasers," *Semicond. Sci. Technol.*, vol. 14, no. 1, pp. 118–123, 1999.

[24] W. W. Chow and F. Jahnke, "On the physics of semiconductor quantum dots for applications in lasers and quantum optics," *Prog. Quantum Electron.*, vol. 37, no. 3, pp. 109–184, May 2013.

[25] H. Wang and D. T. Cassidy, "Gain measurements of Fabry-Pe/spl acute/rot semiconductor lasers using a nonlinear least-squares fitting method," *IEEE J. Quantum Electron.*, vol. 41, no. 4, pp. 532–540, Apr. 2005.

[26] L. J. P. Ketelsen, "Simple technique for measuring cavity loss in semiconductor lasers," *Electron. Lett.*, vol. 30, no. 17, pp. 1422–1424, Aug. 1994.

[27] M. Hammer. (2018). *2-D Multilayer Waveguide Mode Solver Variational Effective Index Approximation*. [Online]. Available: http://www.computational-photonics.eu/eims.html

[28] R. Nagarajan, M. Ishikawa, T. Fukushima, R. S. Geels, and J. E. Bowers, "High speed quantum-well lasers and carrier transport effects," *IEEE J. Quantum Electron.*, vol. 28, no. 10, pp. 1990–2008, Oct. 1992.

[29] T. Chen, B. Zhao, L. Eng, Y. Zhuang, J. O'brien, and A. Yariv, "Very high modulation efficiency of ultralow threshold current single quantum well InGaAs lasers," *Electron. Lett.*, vol. 29, no. 17, pp. 1525–1526, 1993.

[30] J. E. Bowers, "High speed semiconductor laser design and performance," *Solid-State Electron.*, vol. 30, no. 1, pp. 1–11, Jan. 1987.

[31] D. Tauber, G. Wang, R. S. Geels, J. E. Bowers, and L. A. Coldren, "Large and small signal dynamics of vertical cavity surface emitting lasers," *Appl. Phys. Lett.*, vol. 62, no. 4, pp. 325–327, Jun. 1993.

[32] R. Nagarajan, J. E. Bowers, L. A. Coldren, R. S. Geels, T. Fukushima, and M. Ishikawa, "Transport limits in High-speed quantum-well lasers: Experiment and theory," *IEEE Photon. Technol. Lett.*, vol. 4, no. 2, pp. 121–123, Feb. 1992.

[33] K. Y. Lau and A. Yariv, "Ultra-high speed semiconductor lasers," *IEEE J. Quantum Electron.*, vol. QE-21, no. 2, pp. 644–645, Feb. 1985.

[34] M. Kuntz, G. Fiol, M. Laemmlin, C. Meuer, and D. Bimberg, "High-speed mode-locked quantum-dot lasers and optical amplifiers," *Proc. IEEE*, vol. 95, no. 9, pp. 1767–1778, Sep. 2007.

[35] M. G. Thompson, A. R. Rae, M. Xia, R. V. Penty, and I. H. White, "InGaAs quantum-dot mode-locked laser diodes," *IEEE J. Sel. Topics Quantum Electron.*, vol. 15, no. 3, pp. 661–672, May/Jun. 2009.

[36] M. Kajita *et al.*, "Temperature characteristics of a vertical-cavity surface-emitting laser with a broad-gain bandwidth," *IEEE J. Sel. Topics Quantum Electron.*, vol. 1, no. 2, pp. 654–660, Jun. 1995.

[37] G. G. Ortiz, C. P. Hains, B. Lu, S. Z. Sun, J. Cheng, and J. C. Zolper, "Cryogenic VCSELs with chirped multiple quantum wells for a very wide temperature range of CW operation," *IEEE Photon. Technol. Lett.*, vol. 8, no. 11, pp. 1423–1425, Nov. 1996.

David Quandt received the Ph.D. degree in physics from the Technische Universität Berlin in 2018. His current research interest includes the growth of quantum wells and quantum dots and their applications in optoelectronic devices.

Dejan Arsenijević received the Diploma degree in physics from the Technische Universität Berlin in 2009. His current research interests include higher-order modulation formats, and low-jitter optical and electrical pulse sources for future high-speed data communications

André Strittmatter received the Diploma degree in physics from the Technische Universität Berlin (TU Berlin) in 1996, about high-speed MSM photo detectors on InP substrates, and the Ph.D. degree from TU Berlin in 2002. He was involved in GaN epitaxy on Si substrates. His work covers almost the entire III/V semiconductor family with 20+ years of expertise in MOVPE growth of GaP-, InP-, GaAs-, and GaN-related materials. He was the Chief Technological Officer of the Epitaxy Division, Center of Nanophotonics, TU Berlin. He then joined the Palo Alto Research Center (PARC), Palo Alto, CA, USA, where he was involved in semi-polar GaN materials. He returned to TU Berlin in 2010 before he became a Professor with the Otto von Guericke University Magdeburg (OvGU) in 2016, where he is currently the Head of the Semiconductor Epitaxy Department. His work led to the co-invention of over 40 patents. He has coauthored 120+ publications. He has contributed chapters to three books. He is also concerned with the growth of low-dimensional structures such as quantum wells and dots.

Dieter H. Bimberg (M'92–SM'08–F'10–LF'18) was the Chair of the Department of Solid State Physics, Technische Universität Berlin (TU Berlin), from 1991 to 2012. He was the Chair of applied physics until 2015. He was the Founding Director of the Center of Nanophotonics, Technische Universität Berlin. Since 2018, he has been the Director of the Bimberg Chinese–German Center for Green Photonics, Chinese Academy of Sciences, CIOMP, Changchun. He has authored over 1500 papers and 7 books resulting in more than 58,000 citations worldwide and a Hirsch factor of 106 (@ google scholar). He holds 36 patents. His research interests include the growth and physics of nanostructures and nanophotonic devices, ultrahigh speed and energy efficient photonic devices for information systems, single/entangled photon emitters for quantum cryptography, and ultimate nanoflash memories based on quantum dots. He is a Fellow of the American Physical Society in 2004. His honors include the Russian State Prize in Science and Technology in 2001, and his election to the German Academy of Sciences Leopoldina in 2004, the Russian Academy of Sciences in 2011, the American Academy of Engineering in 2014, and the American Academy of Inventors in 2016. He has received the Max Born Award and Medal in 2006, awarded jointly by IoP and DPG, the William Streifer Award of the Photonics Society of the IEEE in 2010, the UNESCO Nanoscience Award and Medal in 2012, the Heinrich–Welker Award in 2015, and the Nick Holonyak jr. Award of OSA in 2018.